Separation Science and Technology
Publication details, including instructions for authors and subscription information:
http://www.informaworld.com/smpp/title~content=t713708471

Behavior of Silica-Supported Manganese Oxides in Hydrometallurgical Separations

Jouni Pakarinen[a]; Markku Laatikainen[a]; Katri Sirola[a]; Erkki Paatero[a]; Risto Koivula[b]; Risto Harjula[b]
[a] Lappeenranta University of Technology, Laboratory of Industrial Chemistry, Lappeenranta, Finland [b] University of Helsinki, Laboratory of Radiochemistry, Helsinki, Finland

To cite this Article Pakarinen, Jouni , Laatikainen, Markku , Sirola, Katri , Paatero, Erkki , Koivula, Risto and Harjula, Risto(2009) 'Behavior of Silica-Supported Manganese Oxides in Hydrometallurgical Separations', Separation Science and Technology, 44: 13, 3045 — 3074
To link to this Article: DOI: 10.1080/01496390903183329
URL: http://dx.doi.org/10.1080/01496390903183329

Separation Science and Technology, 44: 3045–3074, 2009

ISSN: 0149-6395 print/1520-5754 online
DOI: 10.1080/01496390903183329

Taylor & Francis
Taylor & Francis Group

Behavior of Silica-Supported Manganese Oxides in Hydrometallurgical Separations

Jouni Pakarinen,[1] Markku Laatikainen,[1] Katri Sirola,[1] Erkki Paatero,[1] Risto Koivula,[2] and Risto Harjula[2]
[1]Lappeenranta University of Technology, Laboratory of Industrial Chemistry, Lappeenranta, Finland
[2]University of Helsinki, Laboratory of Radiochemistry, Helsinki, Finland

Abstract: The properties of nanoporous manganese oxides for metal uptake from hydrometallurgical solutions were studied. Layer-structured OL-1 and tunnel-structured OMS-1 were synthesized by means of a hydrothermal route and then supported on silica. Competitive uptake of metals and acid was studied using equilibrium, batch kinetic, and fixed-bed measurements. The experimental data were correlated with a dynamic model, which also accounts for the dissolution of the framework manganese. Results show that silica–supported OMS materials can be utilized to separate copper from nickel and cadmium. Behavior of the composites can be explained reasonably well with the presented model and the parameters estimated from the data of the unsupported oxides.

Keywords: Diffusion, ion exchange, metal separation, nanoporous manganese oxides, silica composite

INTRODUCTION

Manganese oxides, having an ordered porous structure, play an important role in soil and aquatic systems and a large number of studies to synthesize and characterize these materials have been carried out (1–7). Manganese coordinates octahedrally with oxygen and by sharing edges

Received 12 February 2008; accepted 12 May 2009.
Address correspondence to Jouni Pakarinen, Lappeenranta University of Technology, Laboratory of Industrial Chemistry, P.O. Box 20, FI-53851 Lappeenranta, Finland. Fax: +358 5 6212199. E-mail: Jouni.Pakarinen@lut.fi

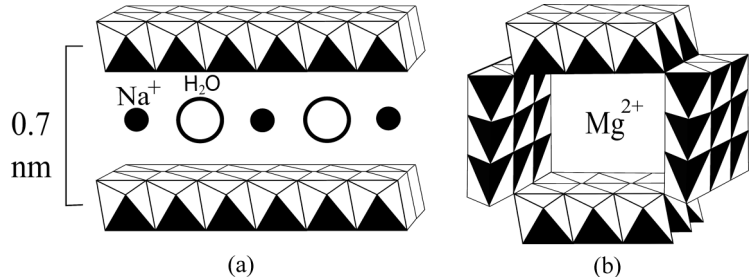

Figure 1. Layer structure of OL-1 (a) and tunnel structure of OMS-1 (b).

and/or corners, these octahedra can form several different tunnel or layered structures (8), called octahedral molecular sieves (OMS). The two- and three-dimensional pore structures of OL-1 and OMS-1 are shown in Fig. 1. The interlayer spacing of OL-1 and the size of the 3×3 tunnels in OMS-1 are both about 0.7 nm (8). The minerals corresponding to OL-1 and OMS-1 are known as birnessite and todorokite.

Due to the presence of Mn^{3+} and Mn^{2+} and vacant octahedra in the $Mn^{4+}O_2$ structure, OMS materials act as ion exchangers. The ion exchange properties of OMS materials have been extensively studied with special attention paid on selective uptake of heavy metals (9,10). For example, Tonkin et al. (11) collected a large amount of literature data on protonation and metal binding of layered manganese oxides (δ-MnO_2 and OL-1). Balakhonov et al. (12) studied the removal of Cs, Pb, and Ba with synthetic H-form OMS-1. Finely divided synthetic or natural oxides have been used in most studies focusing on behavior in natural systems. In only a few cases have supported OMS materials been prepared and used as column packing in order to separate metals from solutions. Han et al. (13) found that zeolite coated with a manganese oxide material (not specified in detail) has strong affinity to Pb^{2+} and Cu^{2+}. Fan and Andersson (14) used activated carbon granules to support β-MnO_2 and found the composites suitable for column separation of Cu^{2+} and Cd^{2+}. Appelo and Postma (15) studied metal uptake with a natural birnessite-type OMS coated on sand. Organic material (polyethylene) as supporting media for birnessite and cryptomelane type OMS material were studied by Liu et al. (16). Lenoble et al. (17) have studied arsenic removal and oxidation with MnO_2 material coated on an anion-exchange resin.

In hydrometallurgical separation metal concentrations are usually much higher than in natural systems and good selectivity for the impurities is needed. The separation material is also expected to be resistant to several loading-stripping cycles in order to make the process economically viable. The objective of this work is thus to assess the suitability of OMS

materials, which can be prepared using inexpensive hydrometallurgical side streams, for column separation. This paper deals with the synthesis of two different types of OMS materials, their characterization and use in metals separation when supported on silica. The materials studied are layer structure OL-1 (birnessite) and tunnel structure OMS-1 (todorokite). The ion exchange equilibria were modeled using the NICA (non-ideal competitive adsorption) (18) isotherm and mass transport in the nanoporous crystals was calculated using the Nernst-Planck equation. In addition to the metal separation properties, reactions involving the Mn framework are also taken into account.

THEORY

Equilibrium Binding Model

Metal loading from the solution to the solid phase is assumed to follow either an ion exchange or redox mechanism. Ion exchange takes place at the negatively charged sites present in the OMS structure. Depending on the synthesis conditions and on subsequent treatments, the framework octahedra may contain small amounts of Mn^{3+} or part of the octahedra may be vacant. The layered OL-1 structure has been reported to contain only a negligible amount of vacancies after synthesis, but the amount increases when the material is dried or treated with acid (19). At the same time, the average Mn oxidation state increases, because a part of the low-valence Mn ions is desorbed. According to Drits et al. (20) and Lei (21), approximately every sixth of the layer Mn sites is vacant in acid-treated H-OL-1. Ion exchange reactions thus take place between the adsorbing cation and three oxygen atoms linked to an octahedral Mn^{3+} or to a vacancy. In the former case, one site has one negative charge while the excess charge of a vacancy site is -2 (15).

Oxide systems are conventionally described using the surface complexation models (SCM) (11,15,22). The applicability of such models to a nanoporous OMS structure is, however, questionable and the model becomes quite complicated when the influence of overlapping double-layers and steric exclusion effects are taken into account. A simpler approach was, therefore, adopted here and the ion-exchange equilibrium is described using a non-ideal competitive adsorption (NICA) model (18) for specific binding at the interlayer or tunnel sites and unselective charge-compensating binding. The explicit form of the NICA isotherm is an important advantage when considering the use of the equilibrium model in dynamic systems (see Section titled ''Dynamic Model'').

The NICA isotherm developed by Kinniburgh et al. (18) offers a thermodynamically consistent way to describe complex competitive adsorption systems. The specifically bound amounts, q_s, of protons and metal cations can be calculated from Eq. (1), where κ and c are the affinity constant and the molar solution concentration. The parameter h depends on the binding stoichiometry and on the lateral interactions of the adsorbed species. The heterogeneity of the sites is characterized by the value p ($0 < p \leq 1$).

$$q_{sp,i} = q_{max}\left(\frac{h_i}{h_H}\right)\frac{(\kappa_i c_i)^{h_i}\left[\sum_j (\kappa_j c_j)^{h_j}\right]^{p-1}}{1+\left[\sum_j (\kappa_j c_j)^{h_j}\right]^{p}} \quad (\mathrm{i,j = H, Me}) \qquad (1)$$

It is assumed here that the maximum proton binding capacity is equal to the total amount of sites, q_{max}. Eq. (1) describes the specific binding on negatively charged sites. However, part of the sites may remain unoccupied and non-specific binding (q_b) is used to compensate the negative charge of these free sites. The equivalent ratio of the non-specifically bound cations is assumed same as in the bulk solution. The total bound amount of cation i is then $q_i = q_{sp,i} + q_{b,i}$. Invasion of anions in the nanopores is considered negligible at the studied conditions.

In this study, ion exchange is assumed to be the only mechanism for binding of cations other than manganese. The manganese oxide framework undergoes, however, changes when the pH of the bulk solution decreases. The extent of these changes depends on the average oxidation state of manganese (AOS), which therefore has great meaning for the material stability. First, Mn^{3+} may disproportionate according to $2Mn^{3+} \leftrightarrows (Mn^{2+} + Mn^{4+}$. A vacancy ($\square$) is also created when Mn^{2+} moves from the framework to interstitial sites and becomes exchangeable. This process can be formally expressed by means of Eq. (2),

$$\begin{aligned} &A^{+}{}_{m}(Mn^{3+}{}_{s}Mn^{4+}{}_{1-s}O_{-2}) + \nu_H H^{+} \overset{K_{dis}}{\rightleftarrows} A^{+}{}_{m'}Mn^{2+} \\ &\quad \times {}_{r}(Mn^{3+}{}_{s'}Mn^{4+}{}_{1-r-s'}\square_{r}\,O_{-2}) + (m-m')A^{+} + 0.5\nu_H H_2O \end{aligned} \qquad (2)$$

where K_{dis} is the apparent equilibrium constant. It is assumed that only a certain fraction of Mn^{3+} undergoes disproportionation and because of the above-mentioned stoichiometry, $r = 0.5(s-s')$. A^+ designates an exchangeable univalent counter-ion and ν_H is considered as an adjustable parameter. According to Feng et al. (8), $\nu_H = 2$ for Li^+ insertion and extraction reactions in spinel–type OMS materials. At sufficiently low pH values

also the four-valent manganese becomes thermodynamically unstable even in the presence of water. Excessively acidic conditions were avoided in this study and, therefore, this effect was not included in the model.

Dynamic Model

Batch Operation

Transport of ions in the layered or tunnel-type manganese oxide micro-crystals was described using the Nernst-Planck equation. No distinction was made between specifically and non-specifically bound species and only the overall values, q, were used for solid concentrations. One-dimensional diffusion is assumed for both structures and in a system of N mobile ions, the flux of ion i, J_i, can thus be given by Eq. (3) (23).

$$J_i = -\rho_s D_{m,i}\left(\frac{\partial q_i}{\partial y} + \frac{z_i F q_i}{RT}\frac{\partial \varphi}{\partial y}\right)$$
$$\frac{\partial \varphi}{\partial y} = -\frac{RT\sum_{j=1}^{N} z_j D_{m,j}\frac{\partial q_j}{\partial y}}{F\sum_{j=1}^{N} z_j^2 D_{m,j} q_j} \tag{3}$$

D_m is the micro-crystalline diffusion coefficient, ρ_s is the material density, z is the ion charge, F is the Faraday constant, and φ is electric potential. R and T have their usual meanings. The potential gradient is obtained from the condition of zero net current ($\sum Z_j J_j = 0$).

The diffusion coordinate is represented by y and depends on the geometry of the crystals (see Fig. 4). OL-1 crystals are approximated as circular discs of diameter d and radial coordinate y. OMS-1 crystals are taken as long fibers with length L, which are open at two ends. In both cases, the faces of the crystals are considered impermeable.

In order to simplify calculations, the solid phase accumulation term appearing in Eq. (3) was evaluated using the approximate solution of Carta and Lewus (23). In the approximate approach, the concentration profiles within the oxide particles are not calculated but the driving force is evaluated approximately from the difference between the surface and average concentrations. The approximate expression for the flux of ion i becomes as follows.

$$J_i \approx -\frac{2 z_i D_{s,i}}{\rho_s d(L)}\frac{[\bar{q}_i - q_i^* \exp(z_i m/5)]}{1 - \exp(z_i m/5)} m \tag{4}$$

In Eq. (4), symbols with an over-bar and an asterisk represent the average and surface values, respectively. Assuming that external mass transfer resistance is negligible and local equilibrium is established at the particle surface, q_i^* is related to the solution concentration by Eq. (1). The parameter m in Eq. (4) is obtained from the condition of zero net current (23) as was shown in Eq. (3) for the potential gradient. The mass balances for the two particle geometries are shown in Eq. (5).

$$\begin{aligned}
&\frac{\partial \bar{q}_i}{\partial t} = -\frac{1}{\rho_s}\left(\frac{4}{d}J_i - \nu_i r_{dis}\right) \quad \text{(OL-1)} \\
&\frac{dc_i}{dt} = \frac{4V_s}{V_{liq}d}J_i \\
&\frac{\partial \bar{q}_i}{\partial t} = -\frac{1}{\rho_s}\left(\frac{2}{L}J_i - \nu_i r_{dis}\right) \quad \text{(OMS-1)} \\
&\frac{dc_i}{dt} = \frac{2V_s}{V_{liq}L}J_i \\
&r_{dis} = k_{dis}\left[q_{Mn3+}^{\alpha} q_{H+}^{\beta} (q^{\theta})^{-(\alpha+\beta)} - \frac{1}{K_{dis}} q_{Mn2+}^{\gamma} (q^{\theta})^{-\gamma}\right] \\
&K_{dis} = \frac{q_{Mn2+}}{q_{Mn3+}^2 q_{H+}^{\nu_H}} (q^{\theta})^{\nu_H+1}
\end{aligned} \tag{5}$$

As shown in the last expressions, disproportionation of Mn^{3+} (Eq. (2)) is accounted for by a simplified solid-phase reaction with a rate constant k_{dis} and an apparent equilibrium constant K_{dis}. The orders were assumed equal to the stoichiometric coefficients; $\alpha = 2$, $\beta = \nu_H$ and $\gamma = 1$. The unit concentration (1 mol/kg) is represented by q^0.

It was assumed on the basis of acid uptake measurements (see Section titled "Binding Kinetics") that mass transport in the silica composites is controlled by diffusion in the OMS crystals. The same equations were thus used to obtain apparent diffusion coefficients for the supported crystals.

Fixed-Bed Operation

The overall mass balance for the fixed-bed system is given by Eq. (6). An axially dispersed flow through the bed is assumed and D_{ax} is the dispersion coefficient. Interstitial flow velocity is represented by u and x is the axial coordinate. Volume fraction of the OMS crystals

is given by η and $\varepsilon_{tot} = 1\text{-}(1\text{-}\varepsilon_p)(1\text{-}\varepsilon_b)$ is the total bed porosity, where ε_b is the bed porosity and ε_p is the pore volume fraction of the silica composite.

$$\frac{\partial c_i}{\partial t} + \frac{\rho_s \eta}{\varepsilon_{tot}} \frac{\partial \bar{q}_i}{\partial t} = -u \frac{\partial c_i}{\partial x} + D_{ax} \frac{\partial^2 c_i}{\partial x^2} \tag{6}$$

Calculations

The NICA parameters were estimated from the titration and sorption equilibrium data. Because of the small number of data points, no fitting procedure was used and the values given were obtained by trial-and-error. Consequently, the parameters are useful for correlation only, and a comparison of individual values is difficult. The differential and arithmetic equations were solved numerically as described in (24). The number of axial grid points was 60 and the time step was typically 1–5 s. Further increase in the number of the grid points did not affect the results.

The initial and boundary conditions were as follows, where c^{init} and c_{feed} refer to the initial and feed concentrations in the batch and fixed-bed experiments, respectively.

Batch:

$$t = 0: \quad c_i = c_i^{\text{init}}, \quad q_i = 0$$

$$t > 0, \quad y = 0: \quad \frac{\partial q_i}{\partial y} = 0$$

Fixed bed:

$$t = 0: \quad c_i = c_i^{\text{init}}, \quad \bar{q}_i = \bar{q}_i^{\text{init}}$$

$$t > 0, \quad x = 0: \quad \frac{\partial c_i}{\partial x} = -\frac{u}{D_{\text{ax}}} (c_{\text{feed},i} - c_i)$$

The axial dispersion coefficient was estimated from known correlations as $5 \cdot 10^{-7}\,\text{m}^2/\text{s}$. A value of 0.4 was used for the bed porosity ε_b. The density of the OMS crystals is taken as 3 g/mL. In all calculations, the changes in the OMS mass were neglected. Highest acid concentration was used in column experiments and even there the amount of Mn removed constituted only 2% of the total OMS mass.

EXPERIMENTAL

Synthesis of OL-1 and OMS-1

The OL-1 synthesis was adapted from the methods of Giovanoli et al. (1) and Feng et al. (2). 400 mL of a $MnSO_4$ solution ($c_{Mn} = 0.6$ mol/L) was poured into a glass reactor with a volume of 1 L. 400 mL of 5 M NaOH solution was added slowly (ca. 4 mL/min) under N_2 atmosphere and under vigorous mixing (600 1/min with a Teflon coated impeller). The temperature was kept below 10°C by an ice water bath and 1.5 L/min of oxygen (AGA, Finland) was fed in the reactor. The duration of each run was 24 h. Finally, the solid was filtered and washed with deionized water until the pH was between 9 and 10. At this stage the product was Na-buserite. The solids were stored in both dry and wet form, but due to easier handling and weighing, most of the experiments were carried out with dry material. However, drying converts the buserite structure to birnessite (OL-1).

Na-buserite was used as the starting material for OMS-1. Washed and centrifuged Na-buserite was first converted to Mg-buserite by MgCl solution ($c_{Mg} = 1$ mol/L) for 24 h under reflux. After refluxing, the solid was washed with deionized water and centrifuged.

Binding of OMS with Silica

Washed and air-dried (moisture content about 70%) OMS material was added into colloidal silica solution (Ludox LS40, Grace Davison) adjusted to pH 4 with 2 M HCl. The mixture was homogenized both by a mechanical stirrer and ultrasonication. OMS material and silica were mixed in a dry weight ratio of 2:3. The mixture was first solidified at 110°C for one hour, crushed, and then heated again at 110°C for another hour. Finally the hard materials were gently ground in a mortar and sieved to the particle size range 125–400 μm. Finally, the composites were heated in air at 250°C for two hours.

Characterization Methods

The structure of the synthesized materials was analyzed using spectroscopic methods, scanning electron microscopy (SEM), N_2 adsorption measurements, and particle size measurements. Crystal structure and purity was verified by means of X-ray powder diffractometry (XRD, PANAnalytical Xpert PRO, and Phillips PW 1710 powder diffractometer with Cu K_α (0.154 nm) radiation). IR spectra were obtained using the standard KBr

tablet method on a Perkin-Elmer 2000 FT-IR spectrometer. SEM images were taken using a JEOL JSM-5800 microscope equipped with an ultra dry X-ray detector from Thermo Fisher Scientific Inc. The pore volume of the OMS/silica composites was measured by water absorption to incipient wetness. The measurement was calibrated using a commercial silica sample (Kieselgel 100, $V_p = 1.1\,mL/g$)). The particle size was analyzed by laser light scattering (Coulter LS130) with ultrasonic pretreatment.

The elemental composition of the synthesized material was analyzed from dissolved samples with plasma emission spectrometry (Iris Intrepid II XDL ICP-AES). The average oxidation state (AOS) of Mn in the synthesized material was determined as follows (5,25). 0.05 M $FeSO_4$ solution was first made and titrated by 0.02 M $KMnO_4$ standard solution. 15 mg of dry MnO material was dissolved in a mixture of 10 mL 0.05 M $FeSO_4$ and 10 mL of 1 M H_2SO_4. The excess Fe^{2+} in the solution was then titrated with the standard $KMnO_4$ solution. The average oxidation state of Mn was calculated from Eq. (7), where V is the volume and c is the molar concentration. M_{Mn} is the molar mass of manganese and w_{Mn} its weight fraction in the solid sample of mass m_{sample}.

$$AOS_{Mn} = 2 + \frac{(V_{FeSO_4}c_{FeSO_4} - 5V_{KMnO_4}c_{KMnO_4})M_{Mn}}{(m_{sample}w_{Mn})} \tag{7}$$

Thermal analysis was used to determine the amount of water and oxygen which evolved from the crystal lattice upon heating. The analyses were carried out using a Netzsch STA 449 C Jupiter analyzer connected to a MS 403C Aëolos Mass Spectrometer. Dry and pulverized samples were heated under He atmosphere to 950°C at a heating rate of 10°C/min.

Dry and finely ground material was titrated in order to clarify their proton and metal ion binding properties. Due to the slow ion exchange kinetics, all materials were titrated in separate batches (glass tubes) and 1 M NaOH and 0.98 HNO_3 solutions were used as reagents. Titrations were carried out in a constant supporting electrolyte ($NaNO_3$) concentration ($I = 0.1$ mol/L) at room temperature. The duration of each experiment was at least 48 hours. Metal titrations were carried out with the same method by replacing a constant amount (0.1 mL) of $NaNO_3$ solution with 0.1 M $Me(NO_3)_2$ solution (Me = Cu or Ni). The total volume of a single batch was 10 mL. The exact amount of each reagent was calculated from the weighed masses and the measured densities (measured with an Anton Paar DMA 4500 density meter). The proton concentration was obtained from the pH measurement by calibrating the pH electrode against known amounts of acid and base at the same ionic strength used in the titration.

Metal binding isotherms on the OMS material were determined for Cu and Ni at a constant supporting electrolyte ($NaNO_3$) concentration ($I = 0.1$ mol/L). 0.15 g of dry material (in base form) was weighed into each batch ($V_{tot} = 40$ mL). The metal uptake was measured by adding a variable amount of 0.1 M $Me(NO_3)_2$ solution and adjusting the pH to 5. Equilibration time was two weeks. The adsorbed amount was calculated from the initial and equilibrium solution concentrations analyzed by means of ICP. As shown in an earlier publication (24), the metal concentrations obtained by this method are correct within 5%. When considering other sources of error, the confidence limits for the equilibrium data are estimated as ±4%.

Acid uptake kinetics was studied using a calibrated glass electrode and an automatic titrator (Titralab TIM856, Radiometer) and a 1 L thermostated glass reactor equipped with a Teflon– coated stirrer. All experiments were carried out at 25°C with 0.1 M $NaNO_3$ as a supporting electrolyte. The initial HNO_3 concentration was 0.01 mol/L and the measurement was started by adding 0.5 g (dry weight) of unsupported OMS or 1.5 g of the supported oxide. The solids were dispersed in a small amount of the background electrolyte solution before addition. Metal binding kinetics was measured in the same reactor using a pH-stat mode. The oxide was first equilibrated at pH 5 for 24 hours before the experiment. Then 10 mL of 0.1 M $Me(NO_3)_2$ was added and samples were taken at certain intervals. Solids were separated from the samples using a membrane filter.

The column experiments were carried out by packing the sieved silica–supported OMS in H-form (particle size 125–400 μm) in a glass column (XK-16, Pharmacia). The bed volume (BV) was 5.0 mL in OL-1 and 9.5 mL in OMS-1 experiments, respectively, and the volumetric feed flow rate in each run was 0.32 BV/min. Acid pulses were run using 0.05 M HNO_3 and base pulses with 0.075–0.13 M NH_4OH. Metal pulses contained Cu, Ni, and Cd at concentrations of 5.2, 5.5, and 5.1 mmol/L. Mn was also present (4.9 mmol/L) in one OL-1 run. The outlet solution was monitored for conductivity and pH, and the metals were analyzed by ICP.

RESULTS

Material Characterization

The synthesized materials were identified by comparing the X-ray diffraction (XRD) profiles and IR spectra with literature data. The XRD profile of Na-OL-1 shown in Fig. 2 agrees well with the reported data (2,3,20,26–31) and no peaks corresponding to the typical impurities hausmannite

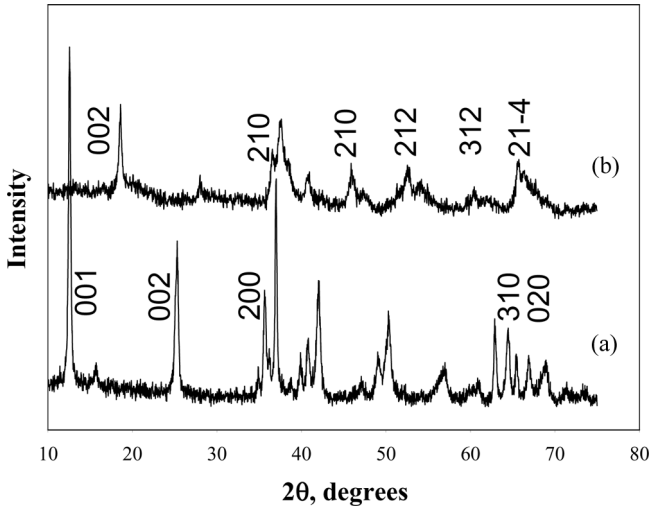

Figure 2. XRD patterns of Na-OL-1 (a) and Mg-OMS-1 (b). Miller indices are according to literature [5, 12, 20].

and feitknechtite (2) were observed. Moreover, the detailed peak pattern at $2\theta = 35$–45^{o} is typical for monoclinic OL-1 (20). The OL-1 structure was also verified by the IR spectrum shown in Fig. 3. The peaks at 425, 477 and 511 cm^{-1} are typical although the intensities may vary depending on the sample source (31). Less literature data are available

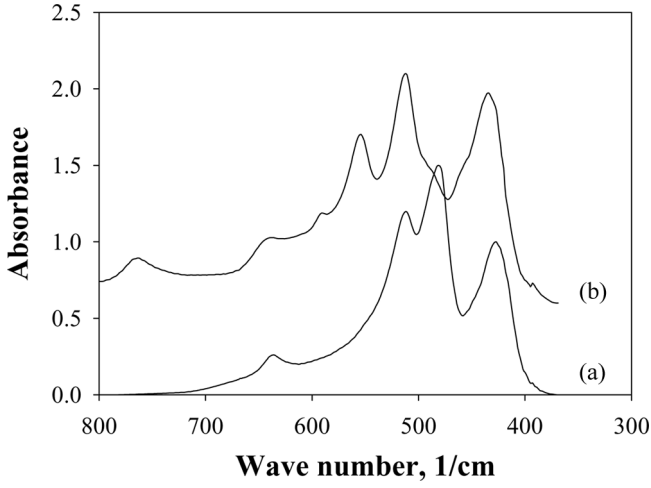

Figure 3. FTIR spectra of Na-OL-1 (a) and Mg-OMS-1 (b).

for OMS-1, but both the XRD and IR spectra measured in this study (Figs. 2 and 3) agree with those reported by Feng et al. (5,29). In particular, the peak at 750 cm^{-1} is characteristic for OMS-1 (31,32). It is also noteworthy that no OL-1 peaks are found in the OMS-1 XRD profile, indicating a complete conversion during the hydrothermal treatment.

The chemical composition of the synthesized materials was estimated from the results of elemental analysis, thermal analysis, and the determination of the average manganese oxidation state (AOS). The average oxidation state of Mn in the synthesized materials was 3.8 for OMS-1 and 3.7 for OL-1. If it is assumed that the manganese exists as Mn^{2+}, Mn^{3+}, and Mn^{4+}, OMS-1 can be represented by the molecular formulas shown below. The bracketed species refer to the oxide framework, while other ions are exchangeable. The left-hand side gives the situation after synthesis and gentle drying, and the right-hand side indicates the composition after acid-induced disproportionation. Equilibrium and kinetic data, which are discussed later, were also needed to determine the relative amounts of Mn^{2+} and Mn^{3+} in OMS-1. The approximate molecular formulas of OL-1 were obtained by similar calculations. Fewer studies were available and, therefore, it was further assumed that one-third of the Mn initially present can disproportionate (19).

$$Mg^{2+}{}_{0.17}, Mn^{2+}{}_{0.022}\,[Mn^{3+}{}_{0.27}Mn^{4+}{}_{0.71}\square_{0.022}O_{\sim 2}]\cdot 2.0H_2O \longrightarrow$$
$$(H^+, \tfrac{1}{2}Mg^{2+}, \tfrac{1}{2}Mn^{2+})_{0.32}[Mn^{3+}{}_{0.20}Mn^{4+}{}_{0.75}\square_{0.057}O_{\sim 2}]\cdot xH_2O \quad \text{(OMS-1)}$$

$$Na^{+}{}_{0.37},\ Mn^{2+}{}_{0.023}\ \left[Mn^{3+}{}_{0.31}Mn^{4+}{}_{0.66}\square_{0.023}O_{\sim 2}\right]\cdot 0.81H_2O \longrightarrow$$
$$\left(H^+, \tfrac{1}{2}Mn^{2+}\right)_{0.36}[Mn^{3+}{}_{0.24}Mn^{4+}{}_{0.70}\square_{0.06}O_{\sim 2}]\cdot xH_2O \quad \text{(OL-1)}$$

The amount of template ions (sodium in OL-1 and magnesium in OMS-1) were somewhat higher than expected. For example, a value of 0.3 mol Na/mol Mn has been reported by Giovanoli et al. (1) and Drits et al. (20) for OL-1. The high counter-ion content may be due to insufficient washing after synthesis. Moreover, when OL-1 was converted to OMS-1, a small amount of Na remained in the structure but it was neglected in the calculations.

In accordance with earlier studies [e.g. 1], OL-1 crystallized as thin plates with an average diameter of 2–5 μm (see Fig. 4a). The thickness of the plates was estimated as 0.2 μm. According to light scattering measurements, the number-average particle size of OL-1 is 0.26 μm. The volume-average size distribution revealed also larger particles formed probably by aggregation of the primary crystals. Distinctly

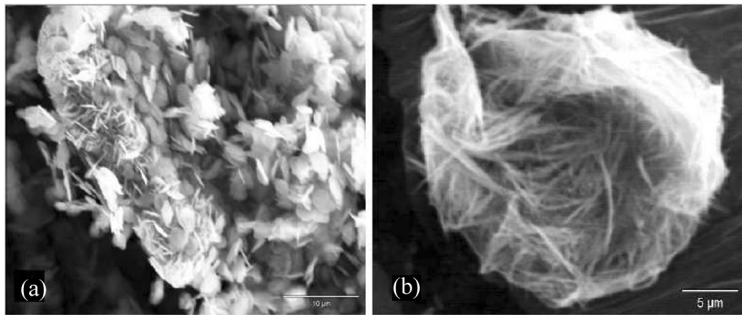

Figure 4. SEM images of Na-OL-1 (a) and Mg-OMS-1 (b).

different crystal shape and dimensions (30) were found for OMS-1, as shown in Fig. 4b. The average length of the rod-like particles was estimated as 10 μm. The aggregation tendency was even stronger for OMS-1, and a high ionic strength seems to enhance aggregation.

The supported manganese oxides were prepared by binding the primary Na-OL-1 and Mg-OMS-1 crystals with silica. It is assumed that the properties of the primary crystals remain unchanged and the only additional parameters of the composite particles are particle size and porosity. The volume-average particle diameter of silica-supported OL-1 and OMS-1 was 340 and 300 μm, as obtained from the light scattering measurement. The pore volumes estimated from water sorption were 0.54 and 0.63 mL/g for OL-1 and OMS-1, respectively. The corresponding particle porosities $\varepsilon_p = 0.58$ and 0.61 were calculated using the density estimated for the OMS/silica composite (2.5 g/mL). These values should be considered as rough estimates only, because of the difficulties in elimination of water sorption by the manganese oxides. However, similar porosities have been obtained in our laboratory for pure silica gels prepared using the same procedure. The pore structure of the Na-OL-1/silica composite is illustrated in Fig. 5.

Ion Exchange Equilibrium

Proton Titrations

The ion-exchange capacities of Na-OL-1 and Mg-OMS-1 and the pH dependence of metal uptake were elucidated by titration. The experimental and calculated acid titration curves are shown in Fig. 6. The number of ion-exchange sites was estimated by curve fitting and the values of 2.3

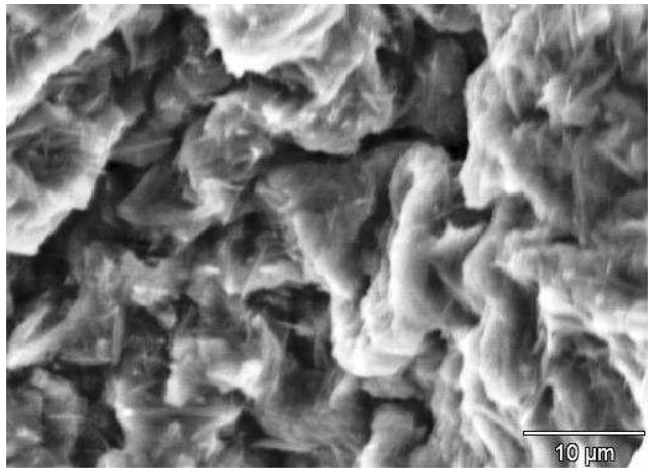

Figure 5. SEM image of silica–supported OL-1.

and 1.9 mequiv/g were obtained for OMS-1 and OL-1, respectively. These values are substantially lower than the analyzed amounts of exchangeable cations, which were 3.0 and 3.5 mequiv/g for Mg-OMS-1 and Na-OL-1, respectively.

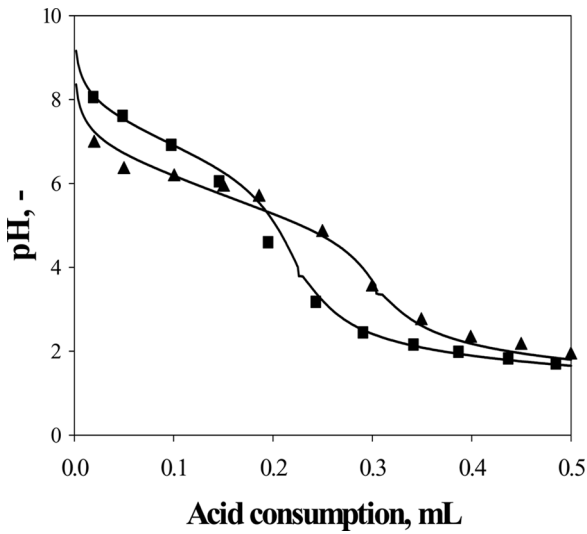

Figure 6. Experimental (symbols) and calculated (solid lines) acid titration curves of OL-1 (squares) and OMS-1 (diamonds). $T = 25°C$, $I = 0.1$ mol/L ($NaNO_3$). The solid lines were calculated from Eq. (1) with the parameters given in Table 1.

Table 1. Equilibrium binding parameters of Eqs. (1) and (2)

	OL-1 $p = 0.2$ $K_{dis} = 1.0$ $\nu_H = 0.5$		OMS-1 $p = 0.2$ $K_{dis} = 3.0$ $\nu_H = 0.5$	
Ion	$\log \kappa$ (κ in L/mol)	h(−)	$\log \kappa$ (κ in L/mol)	h(−)
H^+	7.5	1.0	8.0	1.0
Na^+	1	1.0	1.0	1.0
Mg^{2+}	nd.	nd.	5.0	0.5
Mn^{2+}	3.3	0.50	7.0	0.5
Cu^{2+}	9.6	0.55	36.7	0.15
Ni^{2+}	40.7	0.07	43.7	0.10
Cd^{2+}	8.7[a]	0.4[a]	12.5[a]	0.4[a]

nd.: Not determined.
[a]Values are estimated from break-through data only.

The shapes of the titration curves and the calculated capacities agree well with the data reported by Feng et al. (7,29) for OL-1 and OMS-1. Comparison of the titration data in Fig. 6 suggests that OMS-1 is stronger acid than OL-1. This trend can be seen also from the estimated parameters in Table 1, where the proton affinity coefficient is substantially higher for OL-1. Moreover, the low value of the site heterogeneity parameter, p, indicates a wide acidity distribution in both materials.

Metals Uptake

The effect of pH on metal binding was first studied by titration experiments. The initial concentration of copper and nickel was 1 mmol/L and the obtained pH edges are shown in Fig. 7. For comparison, one experiment was carried out with a Cu concentration of 0.1 mmol/L. The concentrations of Mn and Mg desorbed from OMS-1 during the experiment are also shown in the figure.

According to the results, both materials adsorb Cu from more acidic solutions than Ni ($\Delta pH_{50} > 2$). This sequence is normally observed for several materials and it can be explained by the much stronger coordination of the copper ions to the framework oxygen atoms. However, the behavior of Mn in OMS-1 differs from the usual situation because the binding of manganese and copper takes place in the same pH range. The reason for the enhanced uptake may be the shape and structure of the tunnel sites, which favor manganese. It is important to note, however,

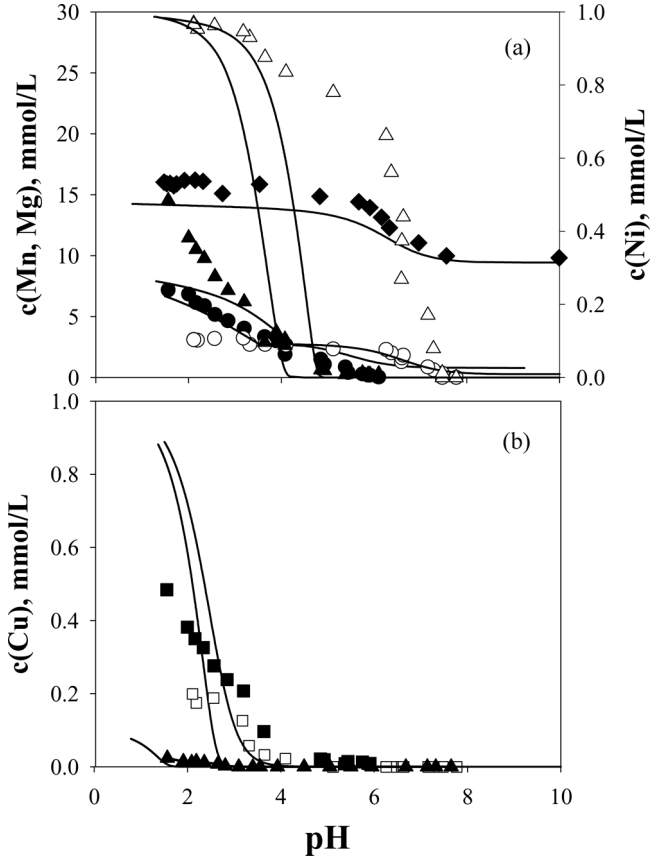

Figure 7. Equilibrium uptake of metals at different pH values. Filled symbols refer to OMS-1 and open symbols to OL-1. (a) Mn (circles), Mg (diamonds), Ni (triangles up, $c_0 = 1$ mmol/L); (b) Cu (squares, $c_0 = 1$ mmol/L) and Cu (triangles up, $c_0 = 0.1$ mmol/L). $T = 25°C$, $I = 0.1$ M ($NaNO_3$). The solid lines were calculated from Eq. (1) with the parameters given in Table 1.

that the manganese curve is also affected by the disproportionation reaction (Eq. (2)). The amount of exchangeable Mn^{2+} increases with decreasing pH and this contribution becomes important below pH 3. The curves in Fig. 7a were calculated with the parameters given in Table 1. The agreement with the experimental data is not very good and, for example, the calculated pH edges of Cu and Ni are much steeper than was found experimentally. Parameter estimation was therefore based largely on other data discussed later. The fraction of Mn^{3+} undergoing disproportionation ($s-s'$ in Eq. (2)) was estimated as 0.09 and 0.08 for OMS-1 and OL-1.

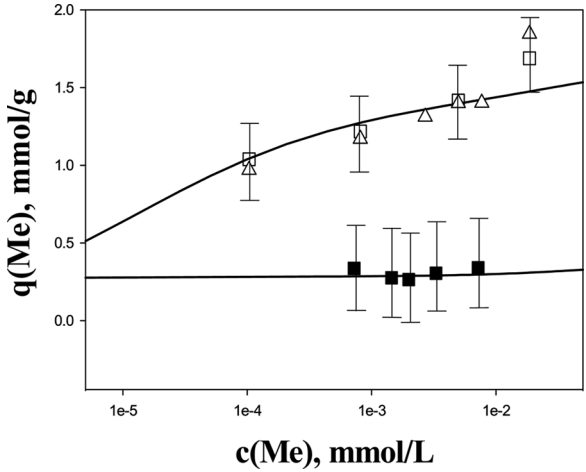

Figure 8. Binding isotherms for copper in OMS-1 (filled symbols) and OL-1 (open symbols) at pH 5. Squares are calculated from solution and triangles from solid respectively. $T = 25°C$, $I = 0.1$ M ($NaNO_3$). The solid lines were calculated from Eq. (1) with the parameters given in Table 1.

Binding isotherms were measured for copper, and the results obtained at 25°C and pH 5 are depicted in Fig. 8. The data were collected at conditions where no precipitation as basic nitrate takes place. The precipitation limit for copper was found to be about 20 mmol/L for the conditions of the experiment. Copper uptake in OL-1 was determined both by solution analysis and by dissolving and analyzing the equilibrated solids. As shown in Fig. 8, both methods gave identical values within the analytical accuracy.

The results show that both oxides have very high affinity for copper. However, the binding capacity of OL-1 is clearly higher than that of OMS-1. The difference is much higher than expected from the ion-exchange capacities. It seems, therefore, that steric exclusion from the narrower tunnel-system of OMS-1 should also be considered. The steric exclusion effects are not explicitly accounted for in the present model, but the low uptake in OMS-1 can be correlated using a very small value for h_{Cu} in Eq. (1). In a similar way, the parameters estimated for Ni from the titration, kinetic, and breakthrough data suggest strong steric exclusion from the tunnel sites. When compared with the values measured by Balakhonov et al. (12) for Pb and Ba, the Cu uptake capacity measured in this study for OMS-1 was about the same. Moreover, the copper capacity of OL-1 is quite similar to the copper uptake of conventional chelating ion exchangers. According to the results of our

laboratory, iminodiacetic acid (IDA) bound on silica or polymer supports binds 0.5–1 mmol Cu/g. Both the studied OMS materials and IDA resins prefer copper over nickel.

Binding Kinetics

Acid uptake kinetics in the synthesized OL-1 and OMS-1 microcrystals was first investigated. The system consists of exchange of the original counter-ions (Na^+, Mg^{2+}, and Mn^{2+}) by H^+ and Na^+ as well as disproportionation of Mn^{3+} according to Eq. (2). Therefore, the exchange process in OMS-1 was also followed by analysis of Mg and Mn concentrations. The experimental data are shown in Fig. 9. The data were correlated with the batch kinetic model (Eqs. (1)–(5)). Because of uncertainties involved in the particle dimensions, the systems can be compared more easily in terms of a lumped parameter defined as $b_m = D_m/d^2$ for OL-1 and $b_m = D_m/L^2$ for OMS-1. The estimated b_m values are given in Table 2.

The results show that acid uptake takes place by displacement of the metal counter-ions and a small contribution of Mn^{3+} dissolution is also present. The rate constant, k_{dis}, in Eq. (3) was estimated as $5.0 \cdot 10^{-2}$ and $2.0 \cdot 10^{-3}$ mol/(Ls) for OL-1 and OMS-1, respectively. The overall exchange rate is largely determined by desorption of the metal cations and no reliable estimate for the proton diffusion coefficient was obtained. The slower rate of OMS-1 is thus mainly due to slower diffusion of divalent Mg^{2+} when compared with univalent Na^+ in OL-1. In view of the complexity of the OMS materials, the simple model gives a reasonable description of the systems.

Similar measurements were also made with the silica-supported materials in order to compare the acid uptake rates. The experimental data shown in Fig. 10 indicate that the exchange rates in unsupported crystals and in macro-porous silica composites were surprisingly similar. The assumption of microcrystalline diffusion control seems to be acceptable for OMS-1, while the contribution of macropore diffusion resistance appears to be significant for OL-1/silica. However, the same simplifying assumption was used for both materials in order to make the calculations easier and faster. The kinetic experiment also showed that mechanical resistance of the silica composites was insufficient to stand prolonged intensive mixing.

Even though the exchange rates were similar, a marked difference was observed in the acid uptake capacities. The proton exchange capacity of OL-1 decreased slightly from 1.9 to 1.7 mequiv/g when supported on silica. On the other hand, only about 1.0 mequiv/g of protons was exchanged in silica-supported OMS-1 and this is less than half of the

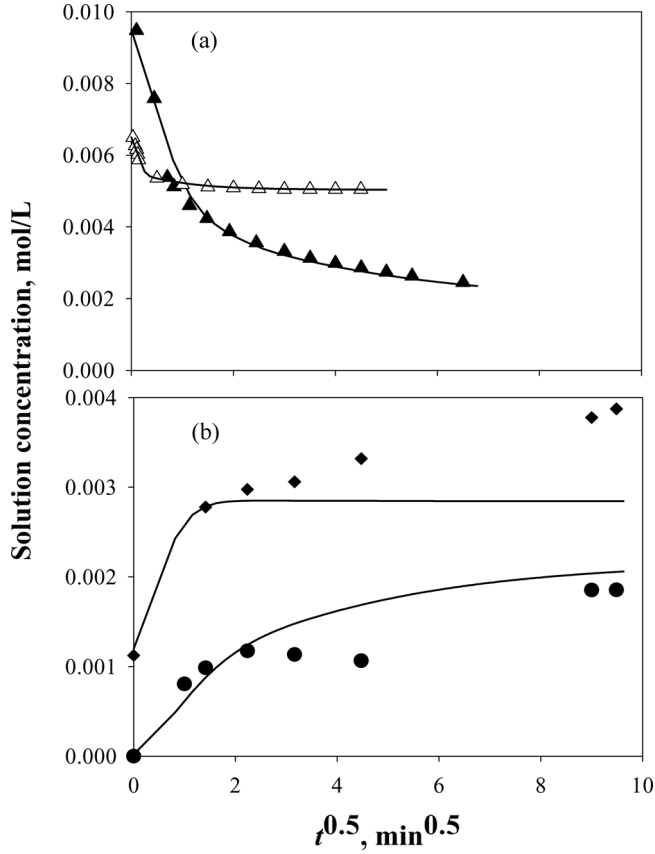

Figure 9. Changes in solution concentrations of H^+ (a) and Mg^{2+} (b, diamonds) and Mn^{2+} (b, circles) during batch acid uptake experiments. $T = 25°C$, $I = 0.1$ M ($NaNO_3$). OMS-1: solid symbols, OL-1: open symbols. Solid lines were calculated from Eqs. (1)–(4) with the parameter values of Tables 1 and 2.

capacity of the original OMS-1. This large difference appears to be due to the heating of the silica composite at 250°C. A similar heating cycle was therefore made for the unsupported material, too, and then the uptake curve was measured again. Before measurement, the material was re-wetted in the supporting electrolyte solution for a week. The capacity decreased irreversibly to 1.1 mequiv/g, which is close to the value obtained for the OMS-1/silica composite. The diffusion rate (not shown) remained, however, practically unchanged.

It is possible that the heat-treatment enhanced the disproportionation of Mn^{3+} and part of the framework manganese was removed in the

Table 2. Mass transport parameter b_m for different cations in unsupported and silica-supported micro-crystals of OL-1 and OMS-1 at 25°C

	b_m (10^{-3} 1/s)			
Cation	OL-1	OMS-1	OL-1/silica	OMS-1/silica
H^+	(40)	(4)	(8)	(4)
Na^+	10	nd.	0.3	1
Mg^{2+}	nd.	0.7	nd.	0.8
Mn^{2+}	2	0.3	0.1	0.2
Cu^{2+}	0.007	0.15	0.01[a]	0.3[a]
Ni^{2+}	0.004	nd.	0.01[a]	0.1[a]
Cd^{2+}	nd.	nd.	0.03[a]	0.1[a]

nd.: Not determined.
[a]Estimated from the break-through data only.

re-wetting step. It has been found (19), that both acid treatment and drying bring about disproportionation in OL-1 and a similar effect can be expected also in OMS-1. Moreover, the heat-treatment decreased the water content in OMS-1 from 14 to 9.3 wt%. At the same time, a marked decrease was observed in the differential thermal analysis (DTA) peak at 150°C and in

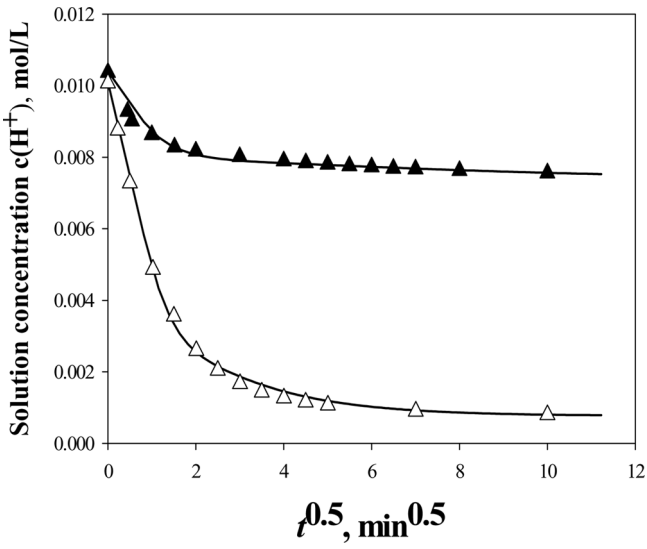

Figure 10. Changes in solution concentration of H^+ during batch acid uptake experiments with silica-supported OMS material. $T = 25°C$, $I = 0.1$ M ($NaNO_3$). OMS-1: solid symbols, OL-1: open symbols. Solid lines were calculated as in Fig. 9.

IR absorptions at 3400 and 1620 cm^{-1}. The IR bands can be assigned to water with a low order of hydrogen bonding (32). The results thus suggest that disordered water is removed irreversibly from the tunnel sites. Changes in tunnel structure are unlikely at 250°C, because the OMS-1 crystals have been reported to be stable up to 600°C (5,29).

Metal uptake kinetics was measured only for unsupported OL-1 and OMS-1. The uptake curves of copper and nickel measured at pH 5 are depicted in Fig. 11. The solid lines represent the calculated uptake curves obtained with the diffusion parameters of Table 2. A comparison of the copper diffusion parameters (Table 2) indicates that the migration in the inter-layer spaces of OL-1 is much more restricted than in the tunnel-shaped pores of OMS-1. On the other hand, no significant difference was observed in the diffusion rates of Ni and Cu in OL-1.

Breakthrough Curves

The properties of the OMS/silica composites in fixed-bed operation were first studied by running three consecutive acid-base pulses through the material. The outlet profiles during the acid pulses in the OMS-1/silica bed are shown in Fig. 12. The calculated curves shown as solid lines were obtained

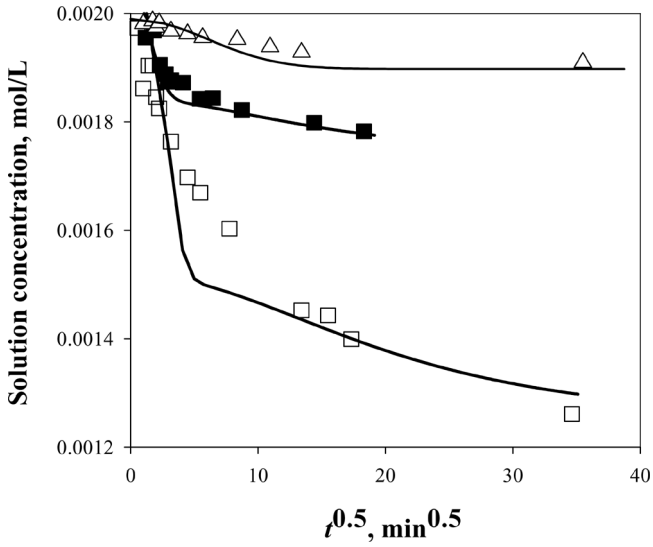

Figure 11. Uptake kinetics of Cu (squares) and Ni (triangles) in OL-1 (open symbols) and OMS-1 (filled symbols) at 25°C and pH 5, $I = 0.1$ M ($NaNO_3$).

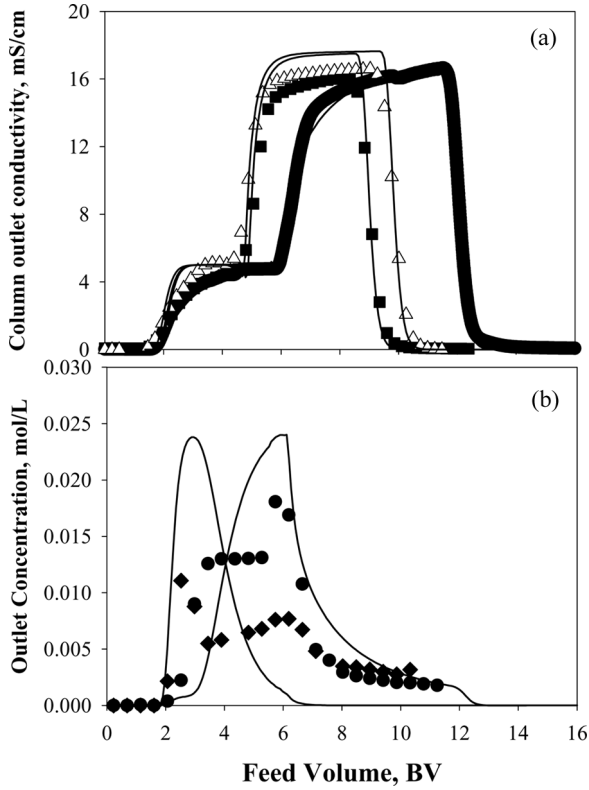

Figure 12. Outlet conductivity of three acid pulses (a: pulse 1: solid diamonds, pulse 2: solid squares, pulse 3: open triangles) and outlet concentration profiles of Mg^{2+} (diamonds) and Mn^{2+} (squares) during pulse 1 (b) in OMS-1/silica bed. $T = 25°C$, BV = 9.5 mL, feed flow rate 0.23 BV/min. Solid lines were calculated from Eqs. (1)–(6).

using Eqs. (1)–(6) and the literature values for equivalent conductivities of the electrolytes involved. The equilibrium parameters estimated for the unsupported oxides were used, but the diffusion parameters were re-adjusted because of the simplified mass transport model (Eq. (6)) used in the fixed-bed calculations. These adjusted values are given in Table 2.

As shown in Fig. 12a, the capacity after the first run decreased about 20%, probably due to the disproportionation of Mn^{3+} and subsequent desorption of Mn^{2+}. Equation (2) shows that dissolution of Mn^{3+} consumes acid and the experimental data suggest that the main part of Mn at oxidation state 3 was dissolved during the first acid pulse. The difference in acid consumption between runs 2 and 3 was only 5%.

The apparent proton uptake capacities estimated from the calculated data were 1.3, 0.9 and 0.8 mequiv/g_{OMS}.

The amounts of displaced magnesium and manganese during the first run were 0.80 and 1.3 mequiv as calculated by integration of the outlet profiles shown in Fig. 12b. The total number of equivalents in the eluted metals closely agrees with the total apparent exchange capacity of the bed (2.2 mequiv in pulse 1). Moreover, the total normality of the displaced cations eluting before the acid front is practically the same as the acid feed concentration. Ion exchange thus appears to be the main mechanism for acid uptake. The marked decrease of acid uptake in pulse 2 indicates, however, that a part of the acid consumption is due to the Mn^{3+} disproportionation reaction (Eq. (2)). If the amount of Mn eluted during pulses 1 and 2 ($1.3 + 0.16$ mequiv) is compared with the difference in the apparent acid uptake ($2.2 - 1.5$ mequiv), the simple balance calculations indicate that about 40% of the eluted manganese stem from the disproportionation reaction.

These findings are in reasonable agreement with the molecular formulas given in the section titled "Material Characterization" and a substantial amount of exchangeable Mn^{2+} thus seems to be present in OMS-1 even before the acid pulse. Moreover, the above reasoning is supported by the model calculations. All the curves were computed using the same ion-exchange capacity of 0.83 mequiv/g_{OMS} and the additional acid consumption can be satisfactorily explained by the Mn disproportionation reaction included in the model. The Mn^{3+} content in the bed was computed after each pulse and this value was used as the starting point for the next pulse. The disproportionation rate constant needed, however, some readjustment and a value $k_{dis} = 6.0 \cdot 10^{-3}$ mol/(Ls) was used instead of $2.0 \cdot 10^{-3}$ mol/(Ls) estimated from the batch kinetic data.

After the last acid pulse and water washing, a pulse containing Cu, Ni, and Cd was loaded in the OMS-1/silica bed. The results of the loading step are shown in Fig. 13a. The metal uptake capacities of the prepared materials were quite small. For example, the final copper loading was 0.14 mmol/g_{OMS}. This value is about half the uptake observed in equilibrium measurements at pH 5 (see Fig. 8). The difference can be explained by considering the pH conditions in the bed. As shown in Fig. 13a, the pH was about 3 under the metal fronts and competition by H^+ thus decreased the metals uptake. At the same time, only a part of the protons initially present in the bed could be displaced by the metals. It seems, therefore, that OMS-1 is too weakly acidic and the whole capacity cannot be effectively utilized in acid-form. The balance between acid and metals uptake is satisfactorily explained by the model, as indicated by the relatively good agreement between the calculated and experimental curves.

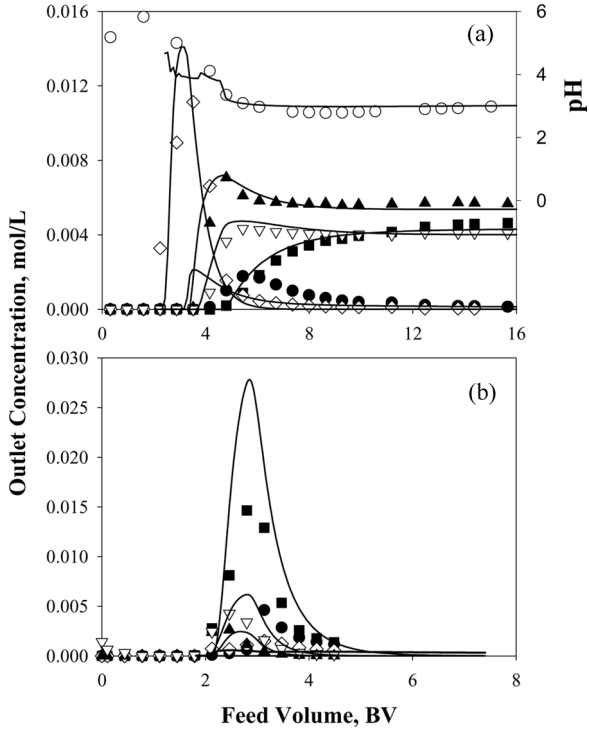

Figure 13. Outlet concentration profiles during the loading (a) and acid elution (b) steps in OMS-1/silica bed. $T = 25°C$, BV = 9.5 mL, feed flow rate 0.23 BV/min. Mn: squares, Cu: open triangles down, Ni: open diamonds, Cd: solid triangles up, pH: open circles. Solid lines were calculated as in Fig. 12.

According to the results, copper can be separated from Ni and Cd, but Mn dissolving from OMS-1 elutes very close to Cu (Fig. 13). The selectivity coefficients $K_{Cu/Ni}$ and $K_{Cu/Cd}$ estimated from the breakthrough results were 21 and 3. The loaded metals were eluted from the bed with 0.05 M HNO_3 and the obtained outlet profiles are depicted in Fig. 13b. The metals desorbed relatively easily and the material was stable enough to endure several runs without marked dissolution. A comparison of the experimental and calculated curves indicates, however, that less copper was actually obtained than was expected on the basis of the loading curve. It seems possible that part of the copper is bound at framework sites and desorption at the studied conditions can be very slow.

A similar metal separation experiment was carried out also with silica-supported OL-1. Results shown in Fig. 14 are qualitatively similar

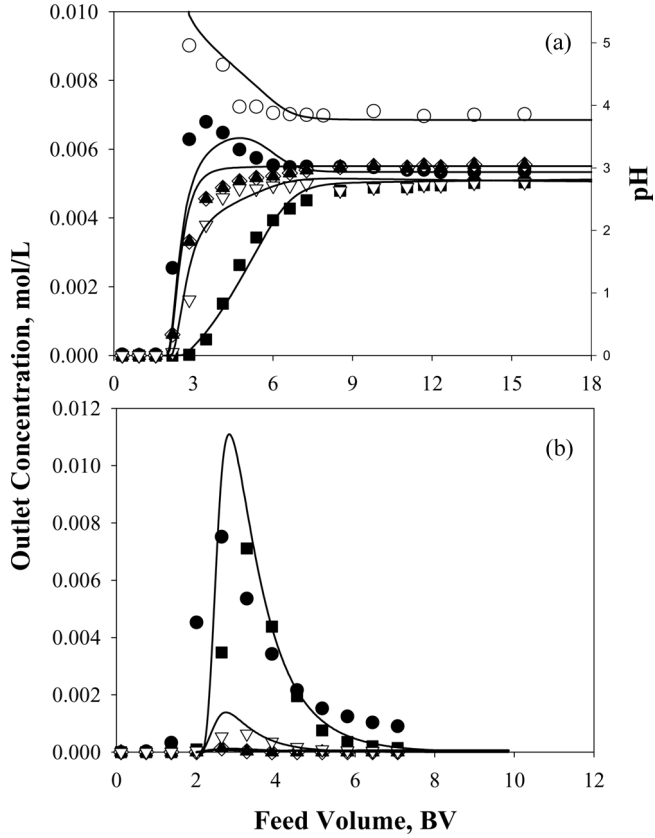

Figure 14. Outlet concentration profiles during the loading (a) and acid elution (b) steps in OL-1/silica bed. $T = 25°C$, BV = 5.0 mL, feed flow rate 0.3 BV/min (loading) and 0.16 BV/min (elution). Mn: squares, Cu: open triangles down, Ni: solid diamonds, Cd: solid triangles up, pH: open circles. Solid lines were calculated as in Fig. 12.

to Fig. 13 but they indicate that the metal capacities of OL-1/silica are even smaller than those of OMS-1/silica. The calculated breakthrough curves were obtained with an exchange capacity 0.4 mequiv/g_{OL}. This result is quite surprising in view of the equilibrium uptake data of the unsupported materials shown in Fig. 8 for copper. It is possible that the low uptake rate of the transition metals in OL-1 (see Table 2) makes part of the material inaccessible during the fixed-bed experiment. The acid elution profiles (Fig. 14b) again show that somewhat less Cu was recovered experimentally than was predicted by model calculations.

Moreover, the large amount of eluted Mn could not be correlated with the proposed model.

The role of the silica support in the observed breakthrough behavior was checked by running acid and metal pulses through a bed of commercial silica gel (Kieselgel 100). The acid uptake was negligibly small in comparison with the OMS/silica composites and practically no metal selectivity was observed. Consequently, the effects observed in Figs. 12–14 can be confidently ascribed to the manganese oxides.

CONCLUSIONS

Two types of OMS manganese oxides, layered OL-1 and tunnel-type OMS-1, were synthesized and supported on silica. The materials were tested for equilibrium metal uptake, uptake kinetics, and for behavior in fixed-bed operations. The results showed the characteristic properties of the manganese octahedral molecular. The experimental data were correlated using the NICA equilibrium model and the Nernst-Planck equation for ion transport in the solids.

The results of the equilibrium and kinetic experiments indicate that both oxides have high affinity for transition metals Cu, Ni, and Cd, and reasonable exchange rates can be attained because of the small particle dimensions. These properties can be utilized in a cyclical fixed-bed operation, when the OMS micro-crystals are supported on porous silica. The breakthrough behavior correlates relatively well with the proposed model thus allowing simulation at different conditions. Some drawbacks inherent to these materials must, however, be taken into account. The exchange capacity of OL-1 and OMS-1 cannot be fully utilized in a simple loading-acid elution cycle, because the materials are too weakly acidic. Moreover, instability at acidic conditions and in the presence of reducing agents limits their use in hydrometallurgical separations. For these reasons, more potential applications for OMS manganese oxides may be found in hydrometallurgical tailings management, in environmental engineering, and in the removal of radio-nuclides.

ACKNOWLEDGEMENTS

Financial support from the Academy of Finland is gratefully acknowledged. The authors also thank Ms. Anne Hyrkkänen for assistance in experimental and analytical work.

LIST OF SYMBOLS

b_m	mass transport parameter, 1/s
BV	bed volume, mL
c	concentration, mol/L
d	average diameter of OL-1 crystals, m
D_m	micro-crystalline diffusion coefficient, m^2/s
D_{ax}	axial dispersion coefficient, m^2/s
F	Faraday constant and
h_i	empirical parameter (Eq. (1))
I	ionic strength, mol/L
J	ion flux, $mol/(m^2s)$
k_{dis}	rate constant of the disproportionation reaction, mol/(Ls)
K_{dis}	equilibrium constant of the disproportionation reaction
L	average length of the OMS-1 crystals, m
m	potential parameter (Eq. (6))
N	number of cations
p	heterogeneity parameter (Eq. (1))
q	amount of adsorbate in the solid phase, mol/kg
q_{max}	total amount of ion exchange sites, mol/kg
r_{dis}	rate of the disproportionation reaction, mol/(Ls)
R	gas constant
t	time, s
T	temperature, K or°C
u	interstitial velocity, m/s
V	volume, L
x	axial coordinate, m
y	diffusion coordinate, m
z	ion charge
□	vacant site

Greek Letters

α, β, γ	reaction orders (Eq. (3))
ε_b	bed porosity
ε_p	intra-particle porosity
ε_{tot}	total bed porosity
κ	affinity constant, L/mol
η	volume fraction of micro-crystals in the bed
ρ	density, kg/L
φ	electric potential, V
ν	stoichiometric coefficient

Subscripts and Superscripts

b	non-specific binding

feed	feed value
H	proton
i, j	ion
init	initial value
liq	liquid phase
p	pore
s	solid phase
sp	specific binding
0	initial value

REFERENCES

1. Giovanoli, R.; Stähli, E.; Feitknecht, W. (1970) Über Oxidhydroxide des vierwertigen Mangans mit Schichtengitter Natriummangan(II,III) manganat(IV), 1.Mitteilung. *Helv. Chim. Acta*, *53*: 209–220. (in German)
2. Feng, X.H.; Liu, F.; Tan, W.F.; Liu, X.W. (2004) Synthesis of birnessite from the oxidation of Mn^{2+} by O_2 in alkali medium: Effects of synthesis conditions. *Clays Clay Minerals*, *52* (2): 240–250.
3. Ma, Y.; Luo, J.; Suib, S.L. (1999) Syntheses of birnessite using alcohols as reducing reagents: Effects of synthesis parameters in the formation of birnessite. *Chem. Mater.*, *11*: 1972–1979.
4. DeGuzman, R.N.; Shen, Y.-F.; Neth, E.J.; Suib, S.L.; O'Young, C.-L.; Levine, S.; Newsam, J.M. (1994) Synthesis and characterization of octahedral molecular sieves (OMS-2) having the hollandite structure. *Chem. Mater.*, *6*: 815–821.
5. Feng, X.H.; Tan, W.F.; Liu, F.; Wang, J.B.; Ruan, H.D. (2004) Synthesis of todorokite at atmospheric pressure. *Chem. Mater.*, *16*: 4330–4336.
6. Ching, S.; Roark, J.L. (1997) Sol-gel route to the tunneled manganese oxide cryptomelane. *Chem. Mater.*, *9*: 750–751.
7. Ching, S.; Krukowska, K.S.; Suib, S.L. (1999) A new synthetic route to todorokite-type manganese oxides. *Inorg. Chim. Acta*, *294*: 123–132.
8. Feng, Q.; Kanoh, H.; Ooi, K. (1999) Manganese oxide porous crystals. *J. Mater. Chem.*, *9*: 319–333.
9. Tsuji, M. (2001) Pb^{2+} separation from concentrated electrolyte solutions by a cryptomelane-type manganic acid and titanium antimonic acid. *Solvent Extract. Ion Exchange*, *19* (3): 531–551.
10. Das, N.; Jana, R.K. (2006) Adsorption of some bivalent heavy metal ions from aqueous solutions by manganese nodule leached residues. *J. Colloid Interface Sci.*, *293*: 253–262.
11. Tonkin, J.W.; Balistrieri, L.S.; Murray, J.W. (2004) Modeling sorption of divalent metal cations on hydrous manganese oxide using the diffuse double layer model. *Appl. Geochem.*, *19*: 29–53.
12. Balakhonov, S.V.; Churagulov, B.R.; Gudilin, E.A. (2008) Selective cleaning of ions of heavy metals from water solutions using the H-form of todorokite synthesized by the hydrothermal method. *J. Surface Investigation, X-ray, Synchrotron Neutron Techniq.*, *2* (1): 152–155.

13. Han, R.; Zou, W.; Li, H.; Shi, J. (2006) Copper(II) and lead(II) removal from aqueous solutions in fixed-bed columns by manganese oxide coated zeolite. *J. Hazardous Mater.*, *B137*: 934–942.
14. Fan, H.-J.; Anderson, P.R. (2005) Copper and cadmium removal by Mn oxide-coated granular activated carbon. *Separ. Purific. Technol.*, *45*: 61–67.
15. Appelo, C.A.J.; Postma, D. (1999) A consistent model for surface complexation on birnessite (δ-MnO_2) and its application to a column experiment. *Geochim. Cosmochim. Acta*, *63* (19/20): 3039–3048.
16. Liu, D.; Teng, Z.; Sansalone, J.J.; Cartledge, F.K. (2001) Surface characteristics of sorptive-filtration storm water media. I.: Low-density ($\rho_s < 1.0$) oxide-coated buoyant media. *J. Environmental Eng.*, *127* (10): 868–878.
17. Lenoble, V.; Laclautre, C.; Serpaud, B.; Deluchat, V.; Bollinger, J.-C. (2004) As(V) retention and As(III) simultaneous oxidation and removal on a MnO_2-loaded polystyrene resin. *Sci. Total Environment*, *326*: 197–207.
18. Kinniburgh, D.G.; van Riemsdijk, H.; Koopal, L.K.; Borkovec, M.; Benedetti, M.F.; Avena, M.J. (1999) Ion binding to natural organic matter: competition, heterogeneity, stoichiometry and thermodynamic consistency. *Colloids Surfaces A*, *151*: 147–166.
19. Silvester, E.; Manceau, A.; Drits, V.A. (1997) Structure of synthetic monoclinic Na-rich birnessite and hexagonal birnessite: II. Results from chemical studies and EXAFS spectroscopy. *Amer. Mineral*, *82*: 962–978.
20. Drits, V.A.; Silvester, E.; Gorshkov, A.I.; Manceau, A. (1997) Structure of synthetic monoclinic Na-rich OL-1 and hexagonal OL-1: I. results from X-ray diffraction and selected-area electron diffraction. *Amer. Mineral.*, *82*: 946–961.
21. Lei, G. (1996) Crystal structures and metal uptake capacity of 10 Å-manganates: An overview. *Marine Geology*, *133*: 103–112.
22. Wang, F.; Chen, J.; Forsling, W. (1997) Modeling sorption of trace metals on natural sediments by surface complexation model. *Environmental Sci. Technol.*, *31*: 448–453.
23. Carta, G.; Lewus, R.K. (1999) Film Model approximation for particle-diffusion-controlled multicomponent ion exchange. *Separ. Sci. Technol.*, *34*: 2685–2697.
24. Sirola, K.; Laatikainen, M.; Lahtinen, M.; Paatero, E. (2008) Separation of copper and nickel from concentrated $ZnSO_4$ solutions with silica-supported chelating adsorbents. *Sep. Purif. Technol.*, *64*: 88–100.
25. Kijima, N.; Yasuda, H.; Sato, T.; Yoshimura, Y. (2001) Preparation and characterization of open tunnel oxide α-MnO_2 precipitated by ozone oxidation. *J. Solid State Chem.*, *159*: 94–102.
26. Cai, J.; Liu, J.; Suib, S.L. (2002) Preparative parameters and framework dopant effects in the synthesis of layer-structure OL-1 by air oxidation. *Chem. Mater.*, *14*: 2071–2077.
27. Ching, S.; Hughes, S.M.; Gray, T.P.; Welch, E.J. (2004) Manganese oxide thin films prepared by nonaqueous sol-gel processing: preferential formation of OL-1. *Microporous Mesoporous Mater.*, *76*: 41–49.

28. Frías, D.; Nousir, S.; Barrio, I.; Montes, M.; López, T.; Centeno, M.A.; Odriozola, J.A. (2007) Synthesis and characterization of cryptomelane- and OL-1-type oxides: Precursor effect. *Mater. Characterization*, *58*: 776–781.
29. Tian, Z-R.; Yin, Y.-G.; Suib, S.L. (1997) Effects of Mg^{2+} ions on the formation of todorokite type manganese oxide octahedral molecular sieves. *Chem. Mater.*, *9*: 1126–1133.
30. Feng, Q.; Kanoh, H.; Miyai, Y.; Ooi, K. (1995) Metal ion extraction/insertion reactions with OMS-1-type manganese oxide in the aqueous phase. *Chem. Mater.*, *7*: 1722–1727.
31. Al-Sagheer, F.A.; Zaki, M.I. (2004) Synthesis and surface characterization of OMS-1-type microporous manganese oxides: Implications for shape-selective oxidation catalysts. *Microporous Mesoporous Mater.*, *67*: 43–52.
32. Potter, R.M.; Rossman, G.R. (1979) The tetravalent manganese oxides: identification, hydration, and structural relationships by infrared spectroscopy. *Amer. Mineral.*, *64*: 1199–1218.
33. Julien, C.M.; Massot, M.; Poinsignon, C. (2004) Lattice vibrations of manganese oxides Part I. Periodic structures. *Spectrochim. Acta A*, *60*: 689–700.